Journal of Materials Chemistry A

COMMUNICATION

Cite this: J. Mater. Chem. A, 2015, 3, 12149

Received 8th April 2015
Accepted 6th May 2015

DOI: 10.1039/c5ta02538a

www.rsc.org/MaterialsA

# A 3D dendritic $WSe_2$ catalyst grown on carbon nanofiber mats for efficient hydrogen evolution†

MeiLing Zou,‡[a] JunFeng Zhang,‡[b] Han Zhu,[a] MingLiang Du,*[a] QingFa Wang,*[b] Ming Zhang[a] and XiangWen Zhang[b]

3D dendritic $WSe_2$ on conductive carbon nanofiber mats (d-$WSe_2$/CFM) was designed and synthesized by a diffusion-controlled CVD method. The d-$WSe_2$/CFM was directly used as a cathode for the HER. The substantially improved HER performance is ascribed to the novel 3D structure with effectively exposed edge sites.

Electrocatalytic production of hydrogen from water splitting has been developed as an effective approach for reducing our reliance on hydrocarbon fuels.[1,2] Various catalysts have been investigated for hydrogen evolution reactions (HERs).[3–5] Although platinum (Pt) or doped Pt catalysts are found to be highly active, the high cost heavily impedes their wide application on a large scale.[6–8] Therefore, a number of alternative catalysts, such as transition metal dichalcogenides (TMDs) $MX_2$ (M = Mo, W and X = S, Se), are being extensively studied since their electrocatalytic activities were identified.[9–12] Both experimental and computational studies have highlighted that the HER activity of TMDs correlates with the active edge sites,[13] consequently, hierarchically constructing TMDs with a high edge fraction is of high importance to improve HER performance. For example, the density of edge sites of 2H $MoS_2$ is highly addressed since it dominates the HER activity while the basal plane is believed to be inert.[14–16] As one of the most promising TMDs, $WSe_2$ has been investigated in the fields of batteries, field-effect transistors, diodes, and so on.[17–20] Recently, the study on $WSe_2$ for the HER has been carried out on the rational design of $WSe_2$ catalysts with more exposure of active edge sites and the results show that nanostructured $WSe_2$ is also a promising and appealing HER electrocatalyst.[12,21] These results motivate us to design hierarchical $WSe_2$ with the aim to enhance its HER performance. However, as far as we know, it is still a great challenge to control the growth of $WSe_2$. In our previous study, the hierarchical structural TMDs were assembled on electrospun carbon nanofiber substrates, exhibiting excellent performance in electrochemical hydrogen evolution applications.[22–24] This communication will provide a more efficient and facile approach to construct a hierarchical $WSe_2$ electrode for the HER with both high effective density of edge sites and high conductive carbon nanofiber mat substrates for the HER.

According to the classical crystal growth theory, dendritic growth, layer-by-layer (LBL) growth and screw-dislocation-driven (SDD) growth are the three basic growth types.[25] Generally, a high supersaturation condition is required for both dendritic growth and LBL growth.[26,27] SDD growth is much more favorable at lower supersaturation than the former ones.[28,29] Under conditions where a rough interface is assumed, such as high supersaturation, the crystal is bounded by rounded non-crystallographic interfaces. If morphological instability occurs on such a rough interface, the crystal takes a dendritic form.[25] The generated structure *via* dendritic growth can, thus, be fully dominated by changing the vapor concentration in the chemical vapor deposition (CVD) process.

In this study, we proposed a method to synthesize 3D dendritic $WSe_2$ with carbon nanofiber mats (CFM) as the conductive substrate by using a CVD method. In this method, the diffusion flux of Se vapor inversely depends on the lateral distance away from the left edge of the furnace.[30] At the upstream of the furnace, the Se vapor concentration is supersaturated, then a rough reaction and growth interface is constructed, leading to morphological instability that occurs on such a rough interface, resulting in the formation of a $WSe_2$ nanostructure with a dendritic crystal structure. However, at the downstream, a rose-like $WSe_2$ nanostructure formed due to the

[a]Key Laboratory of Advanced Textile Materials and Manufacturing Technology of the Ministry of Education, College of Materials and Textile, Zhejiang Sci-Tech University, 310018, P. R. China. E-mail: du@zstu.edu.cn

[b]Key Laboratory for Green Chemical Technology of the Ministry of Education, School of Chemical Engineering and Technology, Tianjin University, 92 Weijin Road, Tianjin, 300072, P. R. China. E-mail: qfwang@tju.edu.cn

† Electronic supplementary information (ESI) available: Experimental details. The EDS analysis and optical image of d-$WSe_2$/CFM. TEM and HAADF-STEM analysis of TS-$WSe_2$/CFM. XRD and Raman characterization of d-$WSe_2$/CFM and r-$WSe_2$/CFM. Photo of the working electrode for d-$WSe_2$/CFM. The magnified SEM images of CFM and $WO_3$/CFM. CV plots of the d-$WSe_2$/CFM electrode at 100 mV $s^{-1}$ for 1000 cycles in 0.5 M $H_2SO_4$. See DOI: 10.1039/c5ta02538a

‡ These authors contributed equally.

reduced driving force caused by the much lower Se vapor concentration. Therefore, the $WSe_2$ nanosheet growth is subject to strong influences of the diffusion of Se vapor through the boundary layer of Ar gas flow. Finally, the generated structures are tailored by the diffusion controlled concentration of Se vapor.

The obtained dendritic $WSe_2$ exhibits a rather low overpotential, a higher current density at −300 mV *vs.* RHE, and a small series resistance for the HER even at a relatively low coverage of $WSe_2$ and low atom fraction of W and Se (Fig. S1†). The excellent HER performance is correlated with the high dense edge sites and the high conductivity of substrates.

The facile CVD approach for $WSe_2$ with different hierarchical structures on CFM is exhibited as below, in which $(NH_4)_6H_2W_{12}O_{40}$ and PAN were selected as the precursors for W and CFM, respectively (see ESI†). Firstly, a W-PAN FM was prepared by electrospinning its DMF solution. Then the W-PAN FM on the boat was transferred to the chamber of a quartz furnace tube. Secondly, a heat treatment was employed to pre-oxide PAN FM and decompose $(NH_4)_6H_2W_{12}O_{40}$ into $WO_3$. Se vapor was then introduced at saturated vapor pressure with Ar. Another heat treatment was applied leading to graphitization of PAN FM and generation of $WSe_2$ by selenization of $WO_3$ and the $WSe_2$ grown on CFM was finally obtained (Fig. S2A†). The boat's lateral distance from the upstream was adjusted in order to adjust the vapor concentration. The synthetic route is illustrated in Fig. 1A. More detailed information about preparation can be found in the ESI.† The obtained CFM with a thickness of 15 μm (Fig. S2B†) exhibit good flexibility and excellent conductivity, and were used as electrodes directly. The $WO_3$ content within fiber decreases significantly after selenization as compared to that within $WO_3$/CFM (Fig. S2C and D†).

Since the vapor concentration of Se can be diffusion-controlled by the lateral distance from upstream, its influence on the generated structure of $WSe_2$ on CFM is illustrated in Fig. 1. A number of flower-like $WSe_2$ in the size of about 2–5 μm were obtained at three positions (Fig. 1A, (a)–(c)). It is interesting to find that three types of microstructures were obtained. Position (a) generated a novel dendritic $WSe_2$ on CFM (Fig. 1B and E), which is defined as d-$WSe_2$/CFM. As shown in Fig. 1D and G, position (c) can grow smooth leaves of $WSe_2$ on CFM with a vivid rose-like shape, which is defined as r-$WSe_2$/CFM. The leaves with bent triangular or hexangular contours can be distinguished for both d-$WSe_2$ (Fig. 1E and S3A†) and r-$WSe_2$ (Fig. 1G and S3C†). The structure generated at the position of (b) exhibited a transition morphology (Fig. 1C and F and S3B†). The sample at position (b) is defined as TS-$WSe_2$/CFM. The structure evolution of $WSe_2$ is suggested to be Se vapor concentration sensitive and could be well diffusion-controlled at different lateral distances from upstream. When the location is close to the upstream, the vapor concentration is believed to be highly supersaturated while a much lower concentration can be achieved at a faraway distance. The adjusted vapor concentrations at different locations thus lead to various structures, which is consistent with the previous report.[31]

The d-$WSe_2$/CFM was fully characterized by TEM, selected area electron diffraction (SAED), high-angle annular dark field (HAADF) STEM, EELS, element mapping and XPS. As shown in Fig. 2A, d-$WSe_2$ branches with 10–80 nm in diameter grew freely and artistically (Fig. 2A). The effective density of edge sites on d-$WSe_2$/CFM is believed to be much higher in comparison to

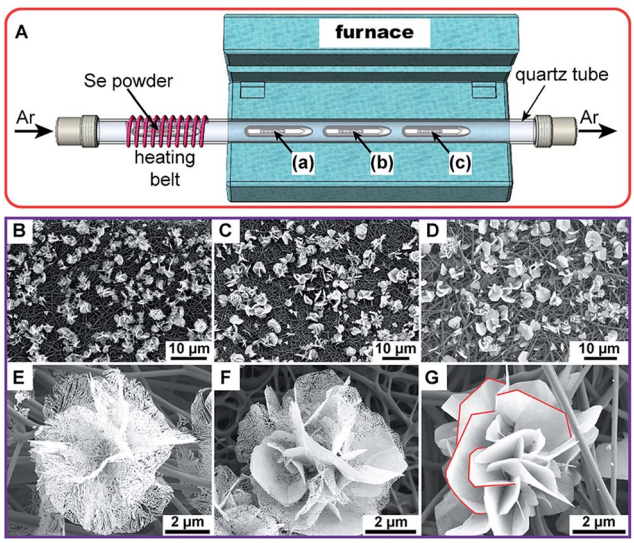


Fig. 1 Schematic illustration of $WSe_2$ growth at different positions in a quartz furnace tube. SEM images of d-$WSe_2$/CFM, TS-$WSe_2$/CFM and r-$WSe_2$/CFM at (B)–(D) low-, as well as (E)–(G) high-magnification at positions (a)–(c) in (A), respectively.

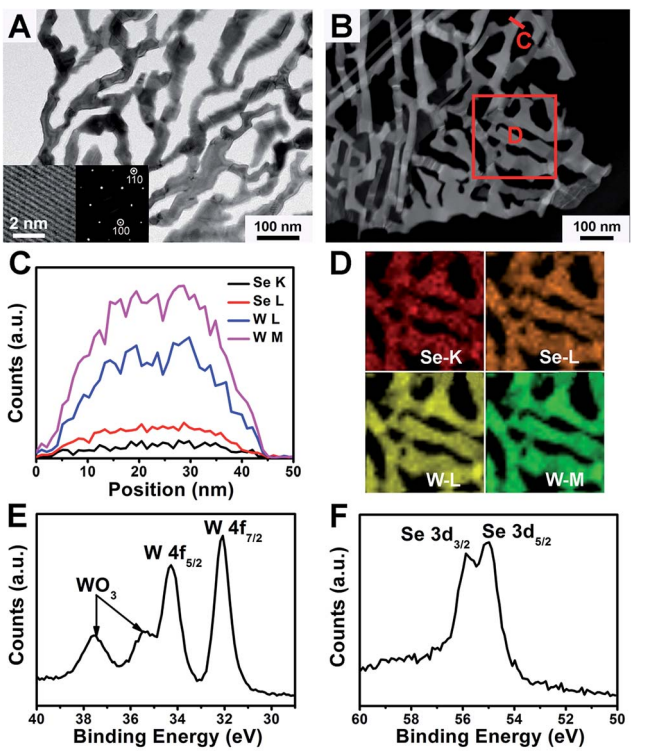


Fig. 2 (A) TEM image of dendritic $WSe_2$ (left inset, HRTEM image; right inset, the corresponding SAED pattern). (B) HAADF STEM images of d-$WSe_2$. (C) The EELS spectra and (D) high-resolution element mapping of the selected region in (B). (E) and (F) XPS analysis of W 4f and S 2p peaks of d-$WSe_2$/CFM, respectively.

that of r-$WSe_2$/CFM. The light and shade contrast indicates the change in the thickness (layer number) of $WSe_2$ branches. The lattice distance observed in the terraces is 3.8 Å (left inset in Fig. 2A), consistent with (100) planes of 2H-$WSe_2$.[32] The SAED pattern (right inset in Fig. 2A) clearly suggests that dendritic $WSe_2$ is configured in the 2H phase,[32] in good accordance with the observed triangular or hexangular morphology in Fig. 1. As shown in EELS (Fig. 2C) and high-resolution element mapping (Fig. 2D), both W and Se elements are homogenously distributed within branches. X-ray photoelectron spectroscopy (XPS) was conducted to investigate the chemical composition of d-$WSe_2$. Two obvious peaks at 34.2 and 32.1 eV (Fig. 2E) are ascribed to W $4f_{5/2}$ and W $4f_{7/2}$, respectively.[33] In Fig. 2F, Se $3d_{5/2}$ and Se $3d_{3/2}$ at 54.2 and 55.0 eV indicate divalent Se ions in good agreement with binding energy values for $WSe_2$ crystals.[33] Additional two weak peaks at around 37.5 and 35.7 eV, correspondingly assigned to W $4f_{5/2}$ and W $4f_{7/2}$, are due to a fraction of $WO_3$ (Fig. S3D†).[33] The TS-$WSe_2$/CFM was also characterized, as shown in Fig. S3E and F.†

The XRD pattern was also employed to evaluate the crystal structure of d-$WSe_2$ and r-$WSe_2$. As shown in Fig. S4,† the diffraction peaks are in consistency with the standard pattern of hexagonal $WSe_2$ (JCPDS card no. 38-1388). The thickness obtained from the full width at half-maximum of (002) according to the Scherrer equation is 1.2 nm, indicating 2 layers of Se–W–Se.[34] The XRD result indicates the same crystal structure of d-$WSe_2$ and r-$WSe_2$. Raman spectroscopy was also exploited to further obtain structural evidence of the catalysts (Fig. S5†). As both $E_{2g}{}^1$ and $A_{1g}$ modes are very close to each other, at 250 and 253 $cm^{-1}$,[21] accordingly, only one peak for $WSe_2$ is observed. The above Raman result for the two hierarchical structures further substantiates the same crystal structure. Two broad peaks at 1354.5 $cm^{-1}$ and 1587.6 $cm^{-1}$ correspond to the D and G band of the CFM. The intensity ratio of D and G bands ($I_D/I_G$) is 1.15. The presence of graphitic structure is expected to achieve a high conductive CFM substrate.[35]

The d-$WSe_2$/CFM was directly used as a hydrogen evolution cathode to highlight the merits of the novel architecture. The configuration of the d-$WSe_2$/CFM electrode is shown in Fig. S6.† CFM, $WO_3$/CFM, $WSe_2$ NPs (Fig. S7†) and r-$WSe_2$/CFM electrodes were also tested as the control. The electrochemical experiment was conducted in a standard three-electrode electrochemical cell setup in 0.5 M $H_2SO_4$ electrolyte. A resistance test was obtained (~8 Ω) *via* electrochemical impedance spectroscopy (EIS) and *iR* compensation was applied. Fig. 3A shows the polarization curves at 5 mV $s^{-1}$ with current density normalized by the geometric surface area. Initial cleaning of the electrocatalyst surface was performed by cycling between 0 and 1.2 V *vs.* RHE at 100 mV $s^{-1}$ for 100 cycles at 25 °C under Ar bubbling. Both d-$WSe_2$/CFM and r-$WSe_2$/CFM show onset HER activity near −150 mV *vs.* RHE, while CFM, $WO_3$/CFM and CVD synthesized $WSe_2$ NPs show negligible HER activity. A current density of 31.7 mA $cm^{-2}$ is achieved at −300 mV *vs.* RHE for d-$WSe_2$/CFM, which is the highest value for $WSe_2$ catalysts to the best of our knowledge as shown in Table S1.†[12,21,36,37] An enhancement in cathodic current density can also be observed

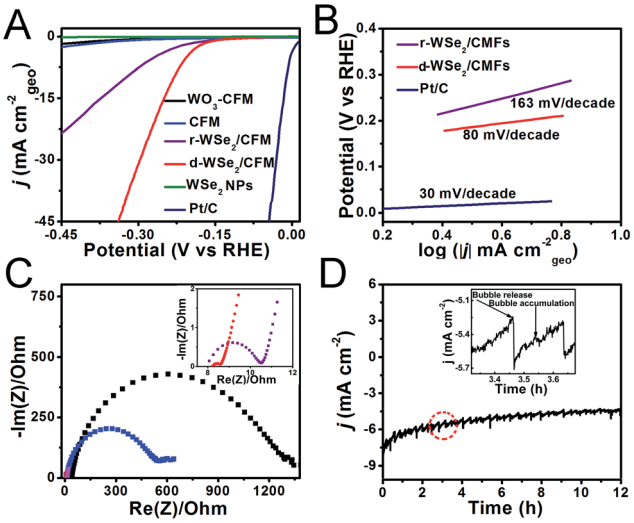


Fig. 3 (A) Polarization curves (after *iR* correction) obtained with several catalysts as indicated. (B) Corresponding Tafel plots for r-$WSe_2$/CFM, d-$WSe_2$/CFM and Pt/C. (C) EIS Nyquist plots collected at a bias voltage of −0.250 V *vs.* RHE. (D) Time dependence of current density under static overpotential of −0.215 V *vs.* RHE. Inset is the enlargement of the area denoted by the dashed circle.

for d-$WSe_2$/CFM as compared to that of r-$WSe_2$/CFM (Fig. 3A), indicating that the dendritic structure is more active since its highly dense edge sites is beneficial for hydrogen evolution. However, r-$WSe_2$ is also a novel structure for $WSe_2$ and may have applications for other research fields. The Tafel slope is associated with the elementary steps in the HER. The first step of the HER is a discharge step (Volmer reaction) in which protons are adsorbed to active sites on the surface of the catalysts and combined with electrons to form adsorbed hydrogen atoms.[21] It is followed by a combination step (Tafel reaction) or a desorption step (Heyrovsky reaction). From the calculated Tafel slope (Fig. 3B), we estimated the rate determining steps of our catalyst. As shown in Table S1,† 80 mV $dec^{-1}$ and 163 mV $dec^{-1}$ were obtained for d-$WSe_2$/CFM and r-$WSe_2$/CFM, respectively. The high Tafel slope (163 mV $dec^{-1}$) of r-$WSe_2$/CFM, similar to the chemical exfoliated $WSe_2$ (120 mV $dec^{-1}$, ref. 36), indicates that the rate-determining step is the discharge step, with a very small surface coverage of adsorbed hydrogen. The significant decrease in the Tafel slope can be observed for d-$WSe_2$/CFM (80 mV $dec^{-1}$), which is attributed to the unique dendritic structure of $WSe_2$ that reduces free energy barrier of the discharge step.[12] The electrochemical double layer capacitance (EDLC) was employed to estimate the active surface areas of the 3D electrodes,[38] as shown in Fig. S8.† The EDLC of d-$WSe_2$/CFM is about 2.6 times larger than that of r-$WSe_2$/CFM, indicating a highly effective surface area of d-$WSe_2$. EIS was also conducted to study the electrode kinetics at −0.25 V *vs.* RHE. The EIS results could well exhibit the advantage of the d-$WSe_2$/CFM quantitatively. As shown in Fig. 3C, Nyquist plots reveal a significant decrease in charge-transfer resistance (RCT) for d-$WSe_2$/CFM (~0.2 Ω) as compared to that of r-$WSe_2$/CFM (~1.2 Ω), $WO_3$/CFM (~610 Ω) and CFM (~260 Ω). The small resistances show the advantage of the facile approach for active

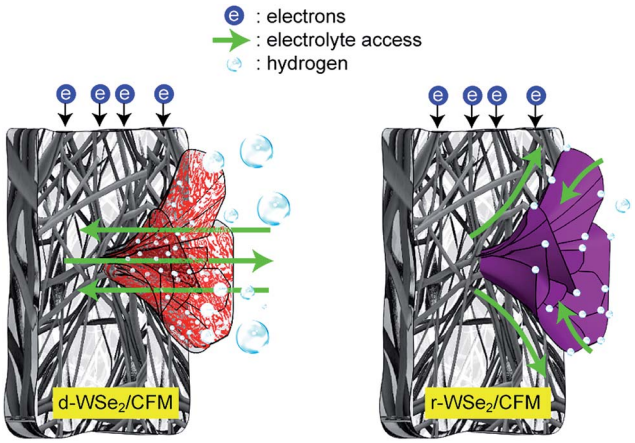


Fig. 4 Schematic illustration of electrochemical behavior of d-$WSe_2$/CFM and r-$WSe_2$/CFM for the HER.

electrocatalysts on conductive substrates, which enables simple and effective electrical integration that minimize Ohmic losses.[39] The HER catalytic activities of d-$WSe_2$/CFM and r-$WSe_2$/CFM are believed to be associated with their different morphologies and electronic properties, which play very important roles in the overall HER performance.[39] The as-synthesized 3D dendritic $WSe_2$ electrode with a small Tafel slope, large available surface area as well as small resistances is a promising candidate for HER applications.

Furthermore, two types of durability tests of d-$WSe_2$/CFM were also conducted. The CV test for 1000 cycles (Fig. S9†) indicated the excellent stability of the electrode. The SEM and TEM images of d-$WSe_2$/CFM after 1000 cycles were also obtained (Fig. S10†). In fact, the morphology and structure of d-$WSe_2$/CFM did not undergo an obvious change after 1000 CV cycles, further indicating the good stability of the catalyst. The other durability test, time dependence of current density at a constant potential for a period of time (Fig. 3D) implied that the current density reaches a constant after an acceptable slight decrease. Although a serrate shape of current was observed that is relative to the alternate processes of bubble accumulation and the bubble release.

The electrochemical behaviors of d-$WSe_2$/CFM and r-$WSe_2$/CFM are illustrated in Fig. 4. Electrons can transfer through the carbon nanofiber to the $WSe_2$ catalyst that have been grown on the CFM. Hydrogen ions at the active sites of the $WSe_2$ catalyst are reduced by the transferred electrons, followed by release of hydrogen gas. For the d-$WSe_2$/CFM, the electrolyte containing hydrogen ions can access a large amount of edge sites through the dendritic structure, leading to much more hydrogen bubbles released from the electrode. r-$WSe_2$/CFM exhibits a relatively poor performance due to the less edge sites on the smooth leaves of $WSe_2$.

## Conclusions

In summary, dendritic $WSe_2$ on conductive CFM was designed and synthesized by a diffusion-controlled CVD method. The d-$WSe_2$/CFM exhibits remarkable enhancement in HER performance due to the effectively exposed edge sites. Moreover, the much lower charge-transfer resistance of d-$WSe_2$/CFM, the high conductivity of carbon nanofiber and the 3D structure are experimentally verified and well correlated with the improvement of HER activity. Above all, a facile method for synthesizing the 3D structural electrode was established. It will open up a new pathway for developing more efficient HER catalysts in the near future.

## Acknowledgements

This work was supported by the National Natural Science Foundation of China (NSFC) (Grant no. 51373154 and 21203137) and the 521 Talent Project of Zhejiang Sci-Tech University.

## References

1 I. Dincer and C. Acar, *Int. J. Hydrogen Energy*, DOI: 10.1016/j.ijhydene.2014.12.035.
2 Y. Zheng, Y. Jiao, M. Jaroniec and S. Z. Qiao, *Angew. Chem., Int. Ed.*, 2015, **54**, 52–65.
3 Y. H. Chang, C. T. Lin, T. Y. Chen, C. L. Hsu, Y. H. Lee, W. Zhang, K. H. Wei and L. J. Li, *Adv. Mater.*, 2013, **25**, 756–760.
4 D. V. Esposito, S. T. Hunt, Y. C. Kimmel and J. G. Chen, *J. Am. Chem. Soc.*, 2012, **134**, 3025–3033.
5 W. F. Chen, J. T. Muckerman and E. Fujita, *Chem. Commun.*, 2013, **49**, 8896–8909.
6 H. H. Li, C. H. Cui, S. Zhao, H. B. Yao, M. R. Gao, F. J. Fan and S. H. Yu, *Adv. Energy Mater.*, 2012, **2**, 1182–1187.
7 X. Cao, Y. Han, C. Gao, Y. Xu, X. Huang, M. Willander and N. Wang, *Nano Energy*, 2014, **9**, 301–308.
8 C. Wang, M. Chi, G. Wang, D. van der Vliet, D. Li, K. More, H. H. Wang, J. A. Schlueter, N. M. Markovic and V. R. Stamenkovic, *Adv. Funct. Mater.*, 2011, **21**, 147–152.
9 S. Shin, Z. Jin, D. H. Kwon, R. Bose and Y. S. Min, *Langmuir*, 2014, **31**, 1196–1202.
10 H. Tang, K. Dou, C. C. Kaun, Q. Kuang and S. Yang, *J. Mater. Chem. A*, 2014, **2**, 360–364.
11 M. A. Lukowski, A. S. Daniel, C. R. English, F. Meng, A. Forticaux, R. J. Hamers and S. Jin, *Energy Environ. Sci.*, 2014, **7**, 2608–2613.
12 K. Xu, F. Wang, Z. Wang, X. Zhan, Q. Wang, Z. Cheng, M. Safdar and J. He, *ACS Nano*, 2014, **8**, 8468–8476.
13 C. Tsai, K. Chan, F. Abild-Pedersen and J. K. Nørskov, *Phys. Chem. Chem. Phys.*, 2014, **16**, 13156–13164.
14 D. Y. Chung, S. K. Park, Y. H. Chung, S. H. Yu, D. H. Lim, N. Jung, H. C. Ham, H. Y. Park, Y. Piao, S. J. Yoo and Y. E. Sung, *Nanoscale*, 2014, **6**, 2131–2136.
15 X. L. Zheng, J. B. Xu, K. Y. Yan, H. Wang, Z. L. Wang and S. H. Yang, *Chem. Mater.*, 2014, **26**, 2344–2353.
16 D. Y. Chung, S. Park, Y. Chung, S. Yu, D. Lim, N. Jung, H. C. Ham, H. Park, Y. Piao, S. J. Yoo and Y. Sung, *Nanoscale*, 2014, **6**, 2131–2136.

 

17 B. Liu, T. Luo, G. Mu, X. Wang, D. Chen and G. Shen, *ACS Nano*, 2013, **7**, 8051–8058.
18 H. Fang, S. Chuang, T. C. Chang, K. Takei, T. Takahashi and A. Javey, *NanoLett.*, 2012, **12**, 3788–3792.
19 R. Cheng, D. Li, H. Zhou, C. Wang, A. Yin, S. Jiang, Y. Liu, Y. Chen, Y. Huang and X. Duan, *Nano Lett.*, 2014, **14**, 5590–5597.
20 W. Zhang, M. H. Chiu, C. H. Chen, W. Chen, L. J. Li and A. T. S. Wee, *ACS Nano*, 2014, **8**, 8653–8661.
21 H. Wang, D. Kong, P. Johanes, J. J. Cha, G. Zheng, K. Yan, N. Liu and Y. Cui, *Nano Lett.*, 2013, **13**, 3426–3433.
22 H. Zhu, M. L. Du, M. Zhang, M. L. Zou, T. T. Yang, S. L. Wang, J. M. Yao and B. C. Guo, *Chem. Commun.*, 2014, **50**, 15435–15438.
23 H. Zhu, M. L. Du, M. Zhang, M. L. Zou, T. T. Yang, Y. Q. Fu and J. M. Yao, *J. Mater. Chem. A*, 2014, **2**, 7680–7685.
24 H. Zhu, F. L. Lyu, M. L. Du, M. Zhang, Q. F. Wang, J. M. Yao and B. C. Guo, *ACS Appl. Mater. Interfaces*, 2014, **6**, 22126–22137.
25 I. Sunagawa, *Forma*, 1999, **14**, 147–166.
26 S. Jin, M. J. Bierman and S. A. Morin, *J. Phys. Chem. Lett.*, 2010, **1**, 1472–1480.
27 G. Zhang, S. Sun, M. Cai, Y. Zhang, R. Li and X. Sun, *Sci. Rep.*, 2013, **3**, 1526.
28 L. Chen, B. Liu, A. N. Abbas, Y. Ma, X. Fang, Y. Liu and C. Zhou, *ACS Nano*, 2014, **8**, 11543–11551.
29 A. Zhuang, J. J. Li, Y. C. Wang, X. Wen, Y. Lin, B. Xiang, X. Wang and J. Zeng, *Angew. Chem.*, 2014, **126**, 6543–6547.
30 C. Li, L. Huang, G. P. Snigdha, Y. Yu and L. Cao, *ACS Nano*, 2012, **6**, 8868–8877.
31 S. Wang, Y. Rong, Y. Fan, M. Pacios, H. Bhaskaran, K. He and J. H. Warner, *Chem. Mater.*, 2014, **26**, 6371–6379.
32 J. K. Huang, J. Pu, C. L. Hsu, M. H. Chiu, Z. Y. Juang, Y. H. Chang, W. H. Chang, Y. Iwasa, T. Takenobu and L. J. Li, *ACS Nano*, 2013, **8**, 923–930.
33 H. Wang, D. Kong, P. Johanes, J. J. Cha, G. Zheng, K. Yan, N. Liu and Y. Cui, *Nano Lett.*, 2013, **13**, 3426–3433.
34 J. Xie, H. Zhang, S. Li, R. Wang, X. Sun, M. Zhou, J. Zhou, X. W. Lou and Y. Xie, *Adv. Mater.*, 2013, **25**, 5807–5813.
35 S. Chen, J. Duan, Y. Tang, B. Jin and S. Z. Qiao, *Nano Energy*, 2015, **11**, 11–18.
36 A. Y. S. Eng, A. Ambrosi, Z. Sofer, P. Šimek and M. Pumera, *ACS Nano*, 2014, **8**, 12185–12198.
37 J. M. Velazquez, F. H. Saadi, A. P. Pieterick, J. M. Spurgeon, M. P. Soriaga, B. S. Brunschwig and N. S. Lewis, *J. Electroanal. Chem.*, 2014, **716**, 45–48.
38 D. S. Kong, H. T. Wang, Z. Y. Lu and Y. Cui, *J. Am. Chem. Soc.*, 2014, **136**, 4897–4900.
39 M. A. Lukowski, A. S. Daniel, F. Meng, A. Forticaux, L. Li and S. Jin, *J. Am. Chem. Soc.*, 2013, **135**, 10274–10277.